Colloids and Surfaces A: Physicochemical and Engineering Aspects 676 (2023) 132152

Contents lists available at ScienceDirect

Colloids and Surfaces A: Physicochemical and Engineering Aspects

journal homepage: www.elsevier.com/locate/colsurfa

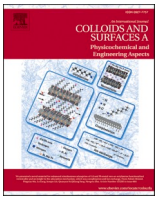

Interactions between γ-alumina surfaces in water and aqueous salt solutions

Olivera Drecun [a], Cecilia Bernardini [b], Misbah Sarwar [b], Alberto Striolo [a,c,*]

[a] Department of Chemical Engineering, University College London, UK
[b] Johnson Matthey Technology Centre, Blount's Ct, Sonning Common, Reading, UK
[c] School of Sustainable Chemical, Biological and Materials Engineering, University of Oklahoma, Norman, OK 73019, United States

GRAPHICAL ABSTRACT

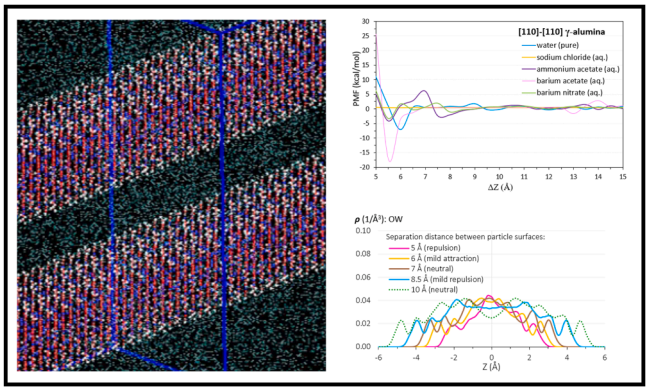

ARTICLE INFO

Keywords:
Potential of mean force
Ion-specific effects
Dynamic light scattering

ABSTRACT

Particle agglomeration is relevant to numerous industrial applications and consumer products. The present work explores interactions between and agglomeration of gamma (γ)-alumina nanoparticles in pure water and dilute aqueous salt solutions. To characterize surface- and salt-specific effects, potential of mean force (PMF) profiles between γ-alumina surfaces ([110] and [100] facets) are extracted using classical molecular dynamics (MD) simulations. Supporting experiments are conducted using dynamic light scattering (DLS) to investigate agglomeration at the macroscale. The ion pairs considered are sodium chloride, ammonium acetate, barium nitrate, and barium acetate; sampling a broad range of the Hofmeister series. As particle surfaces approach contact, free-energy fluctuations of the PMF profiles reflect structural adjustments of the intervening aqueous phase. We extract values for the cohesive energy from the MD results, and parse the resultant effective pair interactions into van der Waals and electrostatic contributions. Molecular scale findings from simulations correlate with hydrodynamic radii of γ-alumina nanoparticles, obtained from DLS experiments. The results highlight the applicability of molecular simulations to identify the origins of macroscale observables.

* Corresponding author at: Department of Chemical Engineering, University College London, UK.
E-mail address: astriolo@ou.edu (A. Striolo).

https://doi.org/10.1016/j.colsurfa.2023.132152
Received 23 May 2023; Received in revised form 17 July 2023; Accepted 28 July 2023
Available online 29 July 2023

1. Introduction

Particulate suspensions are widely utilised in industrial processes and consumer products [1–3]. Particle interactions - and resulting agglomeration behaviours - affect product design, the production process, and product quality [4–7]. Hence, much investigation has been conducted on particle interaction and agglomeration in suspensions, both dilute and concentrated [8–14], as well as the implications for suspension rheology [11,12,15–17]; particularly at high particle volume fractions.

The present work focuses on interactions between gamma (γ)-alumina in pure water, and a selection of dilute aqueous salt solutions. Gamma-alumina was chosen because it has many industrial applications [18], including extensive use as a support material in catalyst coating formulations [19–21], yet studies on γ-alumina nanoparticle agglomeration are few. Among the studies available, the influence of pH and ionic strength on γ-alumina nanoparticle agglomeration have been investigated [22,23], as well as effects due to sonication [24]. Other experimental studies have quantified the influence of pH on the settling behaviour of dilute suspensions [25], dispersion behaviour in water-ethanol mixtures [26], and the effects of pH and stabiliser on sedimentation in water [27]. At finer resolution, two studies [28,29] quantified water-layering on alumina nanoparticle surfaces in suspension, via HAADF-STEM in situ imaging [28] and NMR [29], respectively. The first of these studies [28] showed that the hydration layer around alumina nanoparticle aggregates leads to significant reductions of the available free liquid carrier. NMR results [29] found ordered interfacial water-layering of ~1.4 nm thickness (approximately five water molecules thick) surrounding each nanoparticle. It was postulated that the corresponding increase in effective nanoparticle volumetric fraction could enhance thermal conductivity of the nanofluid. It should be noted that both of these studies refer only to 'alumina' nanoparticles, without specifying the structural polymorph being investigated.

In a recent report, we used molecular dynamics (MD) simulations to examine interfacial hydration structure on isolated surfaces of γ-alumina [30]. Building on those results, we probe here γ-alumina surface interactions in aqueous phases at both molecular and macroscopic resolution, via simulations and experiments, respectively. We consider interactions in pure water, and aqueous solutions of sodium chloride, ammonium acetate, barium acetate (1 molar), and barium nitrate (0.3 molar). The lower concentration of barium nitrate compared to the other aqueous solutions reflects its lower water solubility at ambient conditions [31–33]. Salt concentrations are dilute, but large enough to allow us to probe salt-induced effects, and within the water solubility limit of the various salts. Relevance of the ion pairs to catalyst preparation is explained in prior work [34].

Through the present study we aim to achieve the following: (1) establish the nature of surface interactions in pure water for two predominantly exposed crystallographic terminations of γ-alumina, (2) establish the relative effects of ion pairs in solution on the surface interactions, (3) identify structural adjustments of the aqueous phases between approaching particle surfaces and effects on interaction free energy, and (4) establish whether salt-specific effects observed in the simulation results manifest macroscopically, via experimentally observed particle agglomeration trends. To achieve these aims, we compute potential of mean force (PMF) profiles between γ-alumina surfaces, as a function of surface separation distance. At separations corresponding to features (i.e., maxima and minima) of the PMF profiles, we investigate the changing structural arrangements and distribution of water and ions between the surfaces using atomic density profiles. From the PMF profiles, values for work of cohesion are obtained, and surface interactions are parsed into the contributions from van der Waals and Coulomb potentials. Finally, through comparison of our findings with experimental dynamic light scattering results, we propose trends for the likely probability and range of γ-alumina nanoparticle interactions in the aqueous phases considered.

The remainder of this paper is arranged as follows. Sections 2 and 3 detail our computational and experimental methods, respectively. In Section 4, results are presented and discussed: simulations in Section 4.1, experiments in 4.2. Conclusions are presented in Section 5. Additional material regarding simulation technique, analyses and experimental details are provided in Supplementary Information (SI).

2. Simulation details

2.1. Simulation setup

The two predominantly exposed terminations of gamma-alumina are chosen for this study; crystallographic planes [110] and [100], as denoted by Miller indices. Studies of γ-alumina nanoparticle morphology via DFT simulation [35], neutron diffraction [36], and electron microscopy [37] indicate that the [110] termination comprises 70–83 % of total exposed surface area, followed by the [100] termination, accounting for 17–30 % [35]. We quantify here the interactions between alike surfaces; [110] to [110], and [100] to [100]. For both cases, five aqueous phases are investigated, yielding 10 systems in total. Our aqueous phases are pure water, 1 molar solutions of sodium chloride, ammonium acetate, barium acetate, and 0.3 molar barium nitrate. The comparatively lower concentration of barium nitrate reflects its lower water solubility at ambient conditions [31–33]. Although needed for a rigorously complete picture, interactions of mixed surface type ([110] to [100]) were not simulated because of the extensive computational time required to probe the five aqueous systems considered in this work (see Section 2.3 for more detail). We resort to a weighting procedure, applied to our present results, to approximate the contributions from interactions of mixed surface type in the subsequent discussion.

Our simulation setup comprises two nanoparticles of γ-alumina, within the aqueous phases of interest. Simulation cells, with periodic boundaries in x, y, and z, were set up as shown in Fig. 1. Substrates were positioned with the crystallographic surfaces of interest parallel to the x-y plane. For simulations of the [110] surface, simulation cells of dimensions ~40 * 82 * 102 Å (x, y, z) were set up with between 9531 and 11968 water molecules; the number depending on salt-type and molar concentration. For simulations of the [100] surface, simulation cells of dimensions ~45 * 88 * 128 Å (x, y, z) were set up with between 14702 and 14731 water molecules, depending on salt-type and molar concentration. System sizes of similar average dimensions have been used in prior molecular dynamics (MD) studies for nanoparticle interactions in aqueous solutions [38–40].

2.2. Force fields

2.2.1. γ-alumina

Several structural models have arisen from attempts to characterize the crystal structure of γ-alumina. However, consensus over the accuracy of these structural models has been elusive [41,42]. The most widely adopted model of the γ-alumina unit cell to-date, namely in DFT and ab-initio studies [43–54], is from Digne et al. [35]. This structural model is utilised here, following our prior work [30]. The simulation setup and preparation of γ-alumina nanoparticles as referred to herein is described in SI; Section S1.

Having replicated the unit cell to generate crystal lattices to the desired dimensions, atoms of the nanoparticle crystal structures were subsequently assigned interaction parameters from ClayFF (Clay Force Field) [55]. Surfaces were hydroxylated, following the ab initio study of Wakou et al. [51] yielding ~10.3 and 12.8 OH groups per square nanometre for the [110] and [100] surfaces, respectively. The hydroxylation states considered are representative of acidic pH conditions - frequently encountered in coating formulations [56,57] - at which surface oxygen atoms are mostly protonated. As prescribed by ClayFF, surface OH groups were parameterized with the flexible SPC water

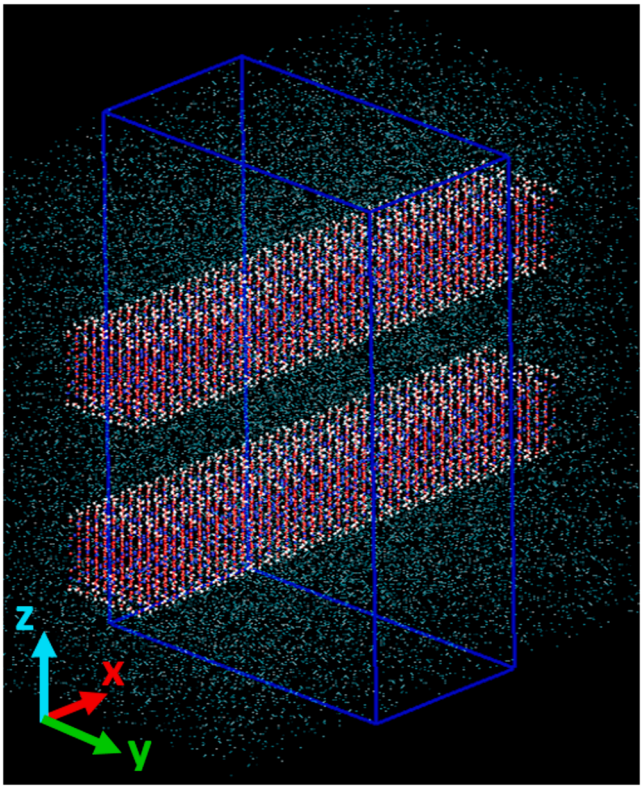

Fig. 1. Representative snapshot of the simulation setup for interaction of γ-alumina surfaces. The blue box is the simulation cell. Inside the cell, two nanoparticles are surrounded by water molecules (cyan). Periodic images are shown extended in the x-direction, in which the particles are effectively infinite, due to the combination of simulation setup and periodic boundary conditions.

model [55]. Geometric mixing rules, as implemented in ClayFF, were applied to calculate Lennard-Jones interaction parameters for unlike atoms (i.e., the interactions between γ-alumina particles and surrounding aqueous phase).

2.2.2. *Water and ion pairs*

The rigid simple point charge extended (SPC/E) water model [58] was utilized to simulate water. O-H bond lengths and the H-O-H angle in each water molecule were maintained rigid using the SHAKE algorithm [59], as implemented in LAMMPS.

Force field parameters developed for use in conjunction with the SPC/E water model were applied to simulate the ion pairs (sodium chloride, ammonium acetate, barium acetate, and barium nitrate) where possible. The forcefield selection is detailed in previous work [34], in which the parameter sets were able to reproduce experimental trends for bulk dynamics of the respective aqueous solutions.

2.3. *Particle interactions: simulation protocol*

Classical molecular dynamics (MD) simulations were conducted using the LAMMPS [60] software package (version 16 Mar 2018). Pair interaction energies are modelled using the Lennard-Jones and Coulomb potentials. Real-space interactions were truncated at 9 Å, while long-range interactions (electrostatics) were treated using a particle-particle-particle-mesh (pppm) solver [61]. Mixed atom-type interactions were calculated from self-interaction parameters, using Lorentz-Berthelot combining rules [62,63]. Equations of motion are integrated over 1 fs time steps, using the velocity-Verlet algorithm [64]. Simulations were conducted with periodic boundary conditions in the canonical ensemble: constant number of particles (N), volume (V) and temperature (T). Temperature is maintained using the Nosé -Hoover thermostat [65,66] at 293.15 K (20 °C); representative of ambient conditions during catalyst coating formulation.

Surface interactions between γ-alumina are analysed by calculating potentials of mean force (PMF) profiles; these are profiles of free energy (reversible work) computed over separation distance. PMF profiles were obtained via the 'umbrella sampling' technique [67,68], using the collective variables module (COLVARS) [69] package in LAMMPS. The procedure implemented for our umbrella sampling simulations is detailed in SI; Section S2. For these simulations, a harmonic biasing potential is used to restrain the position of the upper particle, relative to the lower particle (which is kept fixed), at a specified separation distance. The force-constant value for the harmonic potential (100 kcal/(mol·Å) for most of our simulations) is selected to ensure that oscillatory motion of the upper particle, along the z-coordinate, overlaps sufficiently between adjacent sampling simulations (sampling 'windows'); full details are provided in SI, Section S2. PMF profiles were sampled for interparticle surface separation distances ranging from 25 to 5 Å. The 'surface' reference planes are taken as the surface layer of oxygen atoms of each nanoparticle. Interparticle separation distance was sampled in decreasing increments of 0.5 Å, resulting in 41 umbrella sampling simulations for each system (e.g., γ-alumina [100] surface interactions in pure water; separation distances 25, 24.5, 23 Å…etc). For the 10 systems considered, a total of >400 independent umbrella sampling simulations were conducted, each of 13 ns duration. Adequacy of this duration was tested by obtaining and comparing PMF results for selected systems with simulation times of 6, 13 and 19 ns. Reasonable PMF convergence is attained with umbrella sampling simulations of 13 ns duration; SI, Section S2). To obtain the PMF profiles, unbiased free energies were recovered from the umbrella sampling simulation histograms (obtained from 41 trajectories for each system) using the Weighted Histogram Analysis Method (WHAM) [70,71].

For completeness, it is worth pointing out that each simulation utilised 120 CPU cores with MPI processes, requiring $\leq$ 32 h to complete, depending on the system. Because of the high computational resources required, only interactions between like surfaces ([110]-[110] and [100]-[100]) were quantified explicitly. Quantifying [110]-[100] interactions with the same level of accuracy and for the five aqueous systems considered would require > 200 additional simulations. Future studies will undertake this effort.

With the exception of hydroxyl group hydrogen atoms, nanoparticle atoms are treated as stationary, charged Lennard-Jones (LJ) sites, tethered to their initial position. For atoms of the 'lower' nanoparticle (see, e.g., Fig. 1), this is achieved using the '*fix spring/self*' command in LAMMPS (spring force constant: 100 kcal/(mol·Å), inhibiting translation or rotational motions. For the upper nanoparticle, atoms are allowed to translate (along z-axis coordinates), but not rotate; this constraint is achieved using the '*fix rigid*' command.

3. Experimental methods

3.1. *Particle agglomeration measurements*

Dynamic light scattering (DLS) experiments were conducted to investigate salt-specific influences on agglomeration of γ-alumina nanoparticles. The resolution of this investigative technique requires relinquishing some of the detail available from atomistic simulations. Namely, agglomeration between specific crystallographic faces cannot be parsed. This calls for an assumption that a ~ 70 %, 30 % exposure mix of [110] and [100] faces, respectively [35], represents the surface morphology of γ-alumina nanoparticles used in our experiments. This assumption is consistent with experimental evidence. Indeed, studies of γ-alumina nanoparticle morphology via DFT simulation [35], neutron diffraction [36], and electron microscopy [37] indicate that the [110] termination comprises 70–83 % of total exposed surface area, followed by the [100] termination, accounting for 17–30 % [35].

The DLS technique measures translational diffusion coefficients of

particles undergoing Brownian motion in a suspending medium. The measurement involves the correlation of time-dependent fluctuations in detected light intensity, as light is passed through a sample and scattered by the diffusing particles. The speed of intensity fluctuations depends on diffusion rates; larger particles diffuse more slowly, meaning that correlation of the intensity signal will decay more slowly, and vice versa. The rate of Brownian motion is quantified via the translational diffusion coefficient, D, extracted from the auto-correlation function generated during the measurement. From the value of D, the hydrodynamic diameter (d) of the scattering particle is obtained via the Stokes-Einstein equation [72–74]:

$$D = \frac{k_B T}{3\pi\eta d} \quad (1)$$

In Eq. 1, k_B is the Boltzmann constant, T is the absolute temperature, and η is the viscosity of the suspending medium. The hydrodynamic diameter is defined as the diameter of a hypothetical sphere that diffuses at the same rate as the detected 'particle' (or particle cluster behaving as a single hydrodynamic entity). For the present work, particle agglomeration was analysed using a NanoBrook Omni (Brookhaven Instruments Corporation, USA) DLS analyser; sizing range of 0.3 nm to 10 μm. Light needs to be able to pass through the sample and generate sufficiently strong scattering intensity signals. For this purpose, dilute suspensions (0.05 wt % γ-alumina) were prepared. Measurements were conducted at 20 °C. Complete experimental details are provided in SI (Table S1), and ESI (Excel File).

4. Results and discussion

4.1. Simulation results

The complete set of PMF profiles obtained from our simulations are shown in Fig. 2. Clear overall differences between the PMF profiles obtained for the two γ-alumina terminations are visible. Namely, across the aqueous phases considered, the [110] interactions appear attractive, overall, whereas the interactions for [100] appear more repulsive and somewhat longer ranged, yielding oscillatory profiles. This difference can be explained by comparing the thicknesses of interfacial hydration

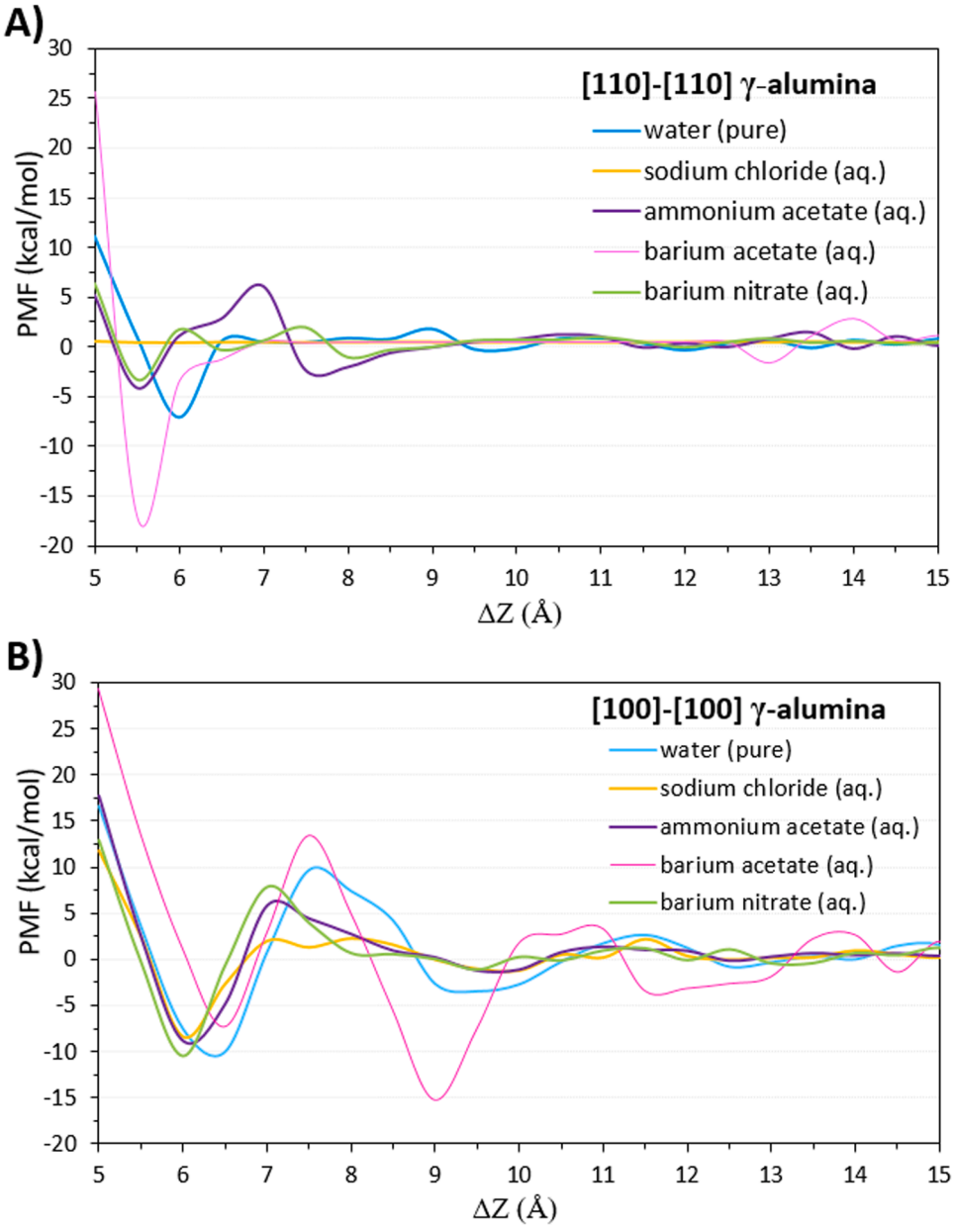

Fig. 2. PMF profiles over particle separation distance, for two prevalent crystallographic surfaces of γ-alumina in pure water and saline aqueous solutions at 1 molar concentration, except for barium nitrate (at 0.3 molar). Panel A: [110]-[110] interactions. Panel B: [100]-[100] interactions. The profiles are obtained from umbrella sampling simulations in the NVT ensemble, at 20 °C. The 'particle separation distance' is the minimum distance between oxygen atoms of the nanoparticle surfaces. PMF profiles over distances up to 25 Å are shown in **SI;** Fig. S4.

structure at the two surfaces, which was detailed in prior work [30]. Interfacial hydration structure was considered at single surfaces of γ-alumina ([110] and [100]); the results showed water more tightly bound to the [110] surface in a spatially narrower interfacial region, compared to a thicker, more diffuse equivalent at the [100] interface [30]. Transferred to the context of two alike surfaces brought into contact, interfacial hydration layers are expected to influence the emergence of repulsive interactions. Two alike surfaces, with hydration structure tightly retained at the solid-liquid interface (e.g., γ-alumina [110]), can approach each other closer before the overlap of hydration layers yields repulsive interactions. It was postulated that the observed atomistic-scale roughness of the [110] surface contributes to formation of less-pronounced interfacial hydration layers, compared to the [100] surface. The resulting differences in interfacial hydration structure further imply that the overall trends of Fig. 2 - notably the 'flatter' (less repulsive) profiles for γ-alumina [110] - ultimately originate from the intrinsic surface characteristics of the crystallographic terminations.

4.1.1. *Surface interactions in pure water*

For both crystallographic terminations considered, the fluctuations of the PMF profiles dominate at separation distances <1 nm. Similar phenomena have been observed for interacting surfaces made of other materials [75,76]. These short-ranged PMF fluctuations, and the separation distances at which they occur, can be correlated to the deconstruction and eventual merging of interfacial hydration layers, as two particle surfaces approach contact [77]. To probe this, Fig. 3 shows atomic density profiles of water (oxygen atoms) confined between [110]-[110] and [100]-[100] surface pairs; panels A and B, respectively. The density profiles are shown at surface separation distances that correspond to main maxima and minima of the PMF profiles, in pure water as the aqueous phase.

As the γ-alumina [110] surfaces are brought together (Fig. 3, Panel

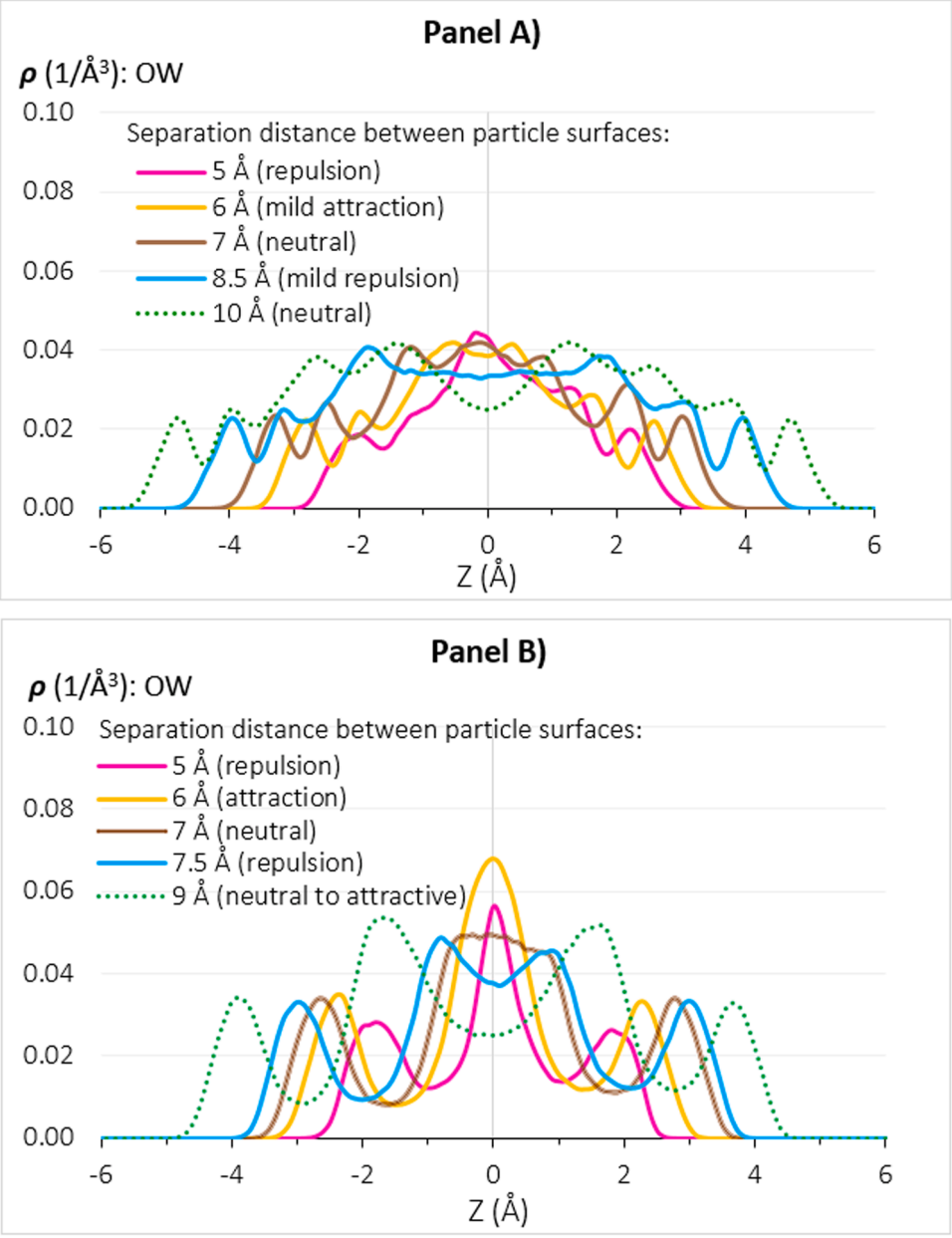

Fig. 3. Atomic density profiles of water (oxygen atoms, 'OW') between γ-alumina surfaces, as a function of surface separation distance, in pure water as the aqueous phase. Panel A: density profiles between γ-alumina [110] surfaces. Panel B: density profiles between γ-alumina [100] surfaces. Density profiles are centrally aligned for ease of interpretation; at each separation distance, Z = 0 is midway between the two surfaces.

A), the water between the two surfaces deconstructs from eight hydration layers (eight density peaks) into seven, five, and then almost three. By contrast, four well-pronounced, more densely populated hydration layers between the γ-alumina [100] surfaces deconstruct into three, via three clear stages: confinement, transition, re-confinement. In the PMF profile between [100] surfaces in pure water (Fig. 2, Panel B), free-energy peaks at 7.5 and 5 Å correlate, respectively, to the well-accommodated hydration layers at 9 and 6 Å squeezing their structure into confinement, rather than sub-dividing into narrower hydration layers. With this mode of adjustment, energetically favourable dynamic configurations for water molecules become limited at the separations of 7.5 and 5 Å. This phenomenon could reduce the local entropy of the solvent between the particle surfaces, yielding the increases in free energy seen in the PMF profile.

4.1.2. *Salt-specific effects on surface interactions*

For both the [110]-[110] and [100]-[100] surface orientations, the ion pairs considered affect the PMF profiles shown in Fig. 2, compared to the results obtained in pure water. The effects are strongly ion-specific. At one end of the spectrum, sodium chloride in aqueous solution reduces the peaks in the PMF profiles, compared to pure water. In fact, the corresponding PMF profile is nearly flat-lined for the γ-alumina [110]-[110] interactions (Fig. 2, Panel A). At the other end of the spectrum, barium acetate enhances the free-energy features (attraction and repulsion) compared to the results obtained in pure water. These opposing influences align with the Hofmeister characteristics of the ion pairs considered, in terms of their described effect on water structure [78], as summarised in Fig. 4. It is also notable that, relative to the PMF profiles in pure water, the ion pairs generally shift the free energy maxima (repulsion) and minima (attraction) positions. This reflects the differing sizes, geometric asymmetries and associated hydration structures of the ion pairs considered; factors which become especially relevant at close particle separation distances. At the closest interparticle separation distance, ~ 5 Å, PMF values for both the [110] and [100] surfaces are, as a consequence, the highest in the aqueous solution of barium acetate; the strongest 'structure-making' ion pair of those considered.

To interpret the salt-specific effects, atomic density profiles of the oxygen atoms of water molecules found between γ-alumina surfaces were obtained, for each of the aqueous salt solutions considered. Complete results are shown in SI; Figs. S5 and S6, respectively. Selected results are shown in Figs. 5 and 6. The results of Fig. 5 show that, between γ-alumina [110] surfaces, water-structuring is enhanced by the presence of barium nitrate and barium acetate in solution. In particular, barium acetate leads to an increase in the atomic density of water (oxygen atoms) between the two surfaces (Fig. 5 and S5), with structural enhancement clearly visible up to 10 Å interparticle separation (Fig. 5, lower panel). As a general observation, ion pairs between [110] surfaces

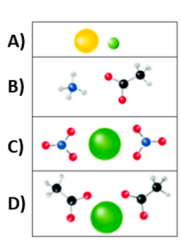

	Hofmeister effect:	Cation	Anion	Hofmeister effect:
A)	'neutral'	Na^+	Cl^-	'neutral'
B)	'structure-breaker'	NH_4^+	CH_3COO^-	'structure-maker'
C)	'structure-maker'	Ba^{2+}	NO_3^-	'structure-breaker'
D)	'structure-maker'	Ba^{2+}	CH_3COO^-	'structure-maker'

Fig. 4. Hofmeister description of the ion pairs considered in the present work, in terms of the described effects on water structure [78]. Rows A, B, C and D show the ion pairs of sodium chloride, ammonium acetate, barium nitrate and barium acetate, respectively. Schematic images of the ion pairs indicate the relative atomic sizes. Radii are taken from an empirical system of unified atomic-ionic radii, suitable for describing anion-cation contacts in ionic structures [79–81].

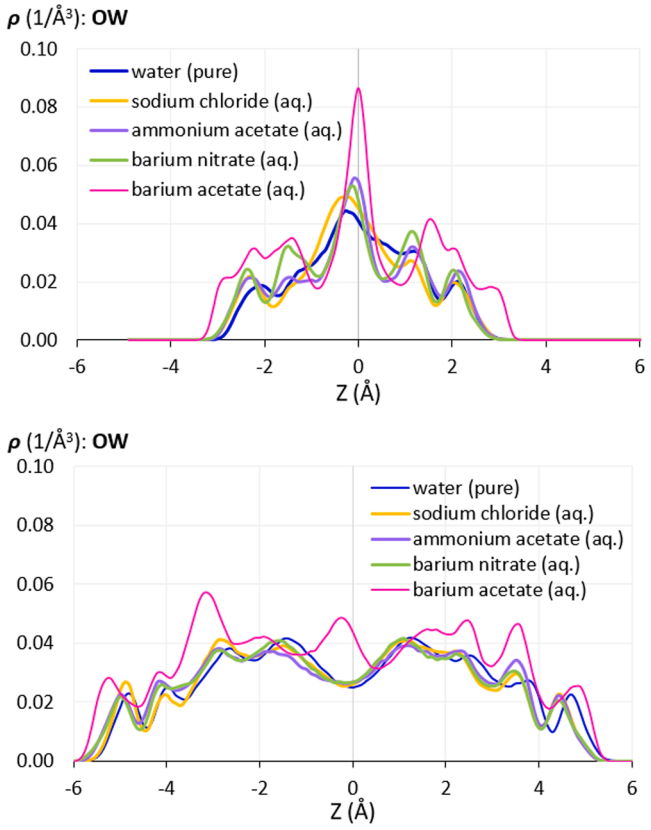

Fig. 5. Atomic density profiles of water (oxygen atoms, OW) between γ-alumina [110] surfaces, as a function of salt type in the aqueous phase. All salt solutions are at 1 molar concentration, except for barium nitrate (0.3 molar). Top panel: 5 Å separation between particle surfaces. Lower panel: 10 Å separation between particle surfaces. Complete results (OW and HW profiles) at separation distances 5, 6, 7, 8.5 and 10 Å are shown in SI; Fig. S5. Density profiles are centrally aligned for ease of interpretation; Z = 0 is midway between the two particle surfaces.

(SI; Fig. S7) are found largely excluded from the immediate surface vicinity (i.e., from the first interfacial hydration layer of each surface), with the exception of ammonium acetate. Between γ-alumina [100] surfaces, the presence of sodium chloride in solution redistributes the water population at the closest interparticle separation distance, 5 Å (Fig. 6, top panel). By contrast, the acetate salts enhance water-structuring. At a surface separation distance of 7 Å (Fig. 6, lower panel), three hydration layers are present between the surfaces. In the case of pure water, the central layer (central peak) is wide, showing the initial stages of splitting into two layers. The presence of barium acetate in solution promotes this split, while the other salts appear to structurally retain the central hydration layer. To explain this, we refer to the PMF profiles between the surfaces of γ-alumina [100] (Fig. 2, panel B). At a surface separation of 7 Å, PMF values for the pure water and barium acetate aqueous phases are near zero. By contrast, profiles for the other aqueous phases yield positive free energy values, to varying extents. This indicates that external energy is required to fuse hydration layers, while the free energy is zero when hydration layers are completely formed. Which of the two outcomes occur depends on the structural compatibility of ion size, local density, and charge distribution with the hydration layers, at any given surface separation distance. It is interesting to note that when the [100] surfaces are at 7 Å separation, most of the ion pairs are largely absent from the central hydration layer, except for barium acetate (SI; Fig. S8). For the latter, the split of the central hydration layer facilitates a more energetically favourable accommodation for the ions (Fig. S8, column 3, Row D); this effect is manifested by some degree of ion pairing, and coordination of the barium ions by water

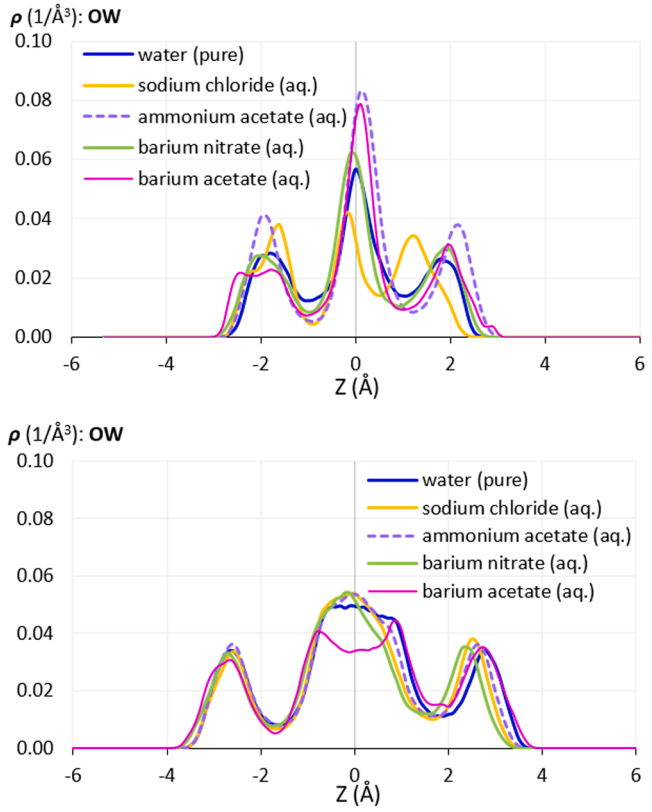

Fig. 6. Atomic density profiles of water (oxygen atoms, OW) between γ-alumina [100] surfaces, as a function of salt type in the aqueous phase. All salt solutions are at 1 molar concentration, except for barium nitrate (0.3 molar). Top panel: 5 Å separation between particle surfaces. Lower panel: 7 Å separation between particle surfaces. Complete results (OW and HW profiles) at separation distances 5, 6, 7, 7.5 and 9 Å are shown in SI; Fig. S6. Density profiles are centrally aligned for ease of interpretation; Z = 0 is midway between the two particle surfaces.

oxygen atoms. This favourable configuration is reflected in the neutral value of the PMF profile for [100] surface interactions, at 7 Å apart, in the aqueous solution of barium acetate (Fig. 2, Panel B).

4.1.3. *Electrostatic and dispersive contributions to surface interactions*

Quantification of particle interactions in aqueous electrolyte solutions, on the colloidal scale, is often discussed in the framework of Derjaguin-Landau-Verwey-Overbeek (DLVO) theory [82,83]. DLVO ascribes interactions of alike particles to a combination of predominantly repulsive electrostatic potential, arising from an 'electrostatic double--layer' of ions around the particles, and attractive van der Waals interactions. These two potential energy contributions comprise the total potential energy of the colloidal system. According to the theory, the double-layer force stabilizes a suspension, while the van der Waals force promotes agglomeration. At separations <2 – 4 nm, the latter is often dominant, and leads to adhesive contact [84]. However, ultimate particle contact additionally involves hydration forces, 'short-ranged' in their influence [85,86]. These forces – not incorporated by DLVO – arise from the overlap, rearrangement, and breakdown of aqueous molecular structure between approaching particle surfaces, as examined in the previous sections.

To relate our results to the DLVO framework, Fig. 7 shows γ-alumina surface interactions, parsed into contributions from van der Waals and Coulomb energies, across the differing aqueous phases. Values were computed during the simulations using the *'compute group/group'* command in LAMMPS [60,87]. The results represent the total dispersive and total electrostatic interaction energies considered solely between γ-alumina particles, ignoring anything else (e.g., water and ions), as a function of surface-surface separation distance. Fig. 7 shows stronger electrostatic repulsion between γ-alumina [100] surfaces, compared to [110]. This can be attributed to a higher surface density of OH groups for the [100] surface (12.9 compared to 10.3 OH/nm^2). For both [110]-[110] and [100]-[100] interactions, the presence of ion pairs increases Coulomb repulsive energies between particle surfaces, although the effect is broadly similar for all the ion pairs considered, when computational uncertainties are taken into account. This result could be due to a few reasons. Dynamic reorientation of γ-alumina surface OH groups, induced via interaction with ions, could lead to stronger surface-surface repulsions. This possibility is examined in SI (Section S9). The results show small differences in the orientation of surface OH groups due to the presence of the ions. It is also observed that the ion pairs with the strongest effect on the electrostatics in Fig. 7 (Panel B), i.e., sodium chloride and ammonium acetate, reside closer to the surfaces than the other ion pairs considered. Representative simulation snapshots showing ion pairs between the two surfaces of [110], and [100], are presented in SI; Section S10. While the changes in surface-group orientation may appear small for the differences in Fig. 7, the cumulative effect is significant, as suggested by the results in SI, Section S11a, which show electrostatic interactions between γ-alumina surfaces in vacuum. Particularly for γ-alumina [110], a clear trend can be seen whereby the surface groups turn away from the opposing surface in vacuum, compared to their orientation in water (SI, Section S11b). A more conservative response is seen for γ-alumina [100], with only the surface groups closest to the bulk structure affected; namely Al_6O_3H. Conventional wisdom suggests that electrostatic repulsion between charged surfaces should be higher when separated by vacuum, compared to water, since the latter medium has a higher dielectric constant (i.e., screens more of the charge). However, this reasoning doesn't account for possible adaptive surface responses to minimise repulsion, depending on dielectric characteristics of the intervening medium.

Another contribution to increased electrostatic repulsion could be the 'dielectric decrement' effect [88–90], whereby the dielectric constant of a solvent diminishes as ionic concentration is increased. Solvents with high dielectric constant (such as pure water) have greater ability to screen the interactions between charged particle surfaces. In aqueous solution, the addition of ions decreases this capability via ion-induced structural modification of the solvent (i.e., ion hydration shells) and ionic polarizability [90]. Because our models have fixed charges, the latter mechanism cannot be probed adequately herein.

4.1.4. *Simulation results: interparticle work of cohesion*

To relate the PMF profiles to macroscopic properties, work of cohesion ($W_{cohesion}$) values were derived from the PMF profiles, in each of the aqueous phases considered. By differentiation of the PMF profiles, force-distance curves were estimated, via the relation $\langle F(r)\rangle = -[d(PMF(r))/d(r)]$. Values for $W_{cohesion}$ were then obtained by integrating the force-distance curves (see SI; Section S12) and normalized by the interfacial area of each surface pair (SI, Section S12; Tables S3 and S4).

Because [110] and [100] terminations comprise ~70–83 and 17–30 % of exposed surface area in experimental systems, respectively [35–37], the reported $W_{cohesion}$ values are obtained by weighting the separate $W_{cohesion}$ results of [110]-[110] and [100]-[100] interactions (details in SI; Section S13). In our approach, it is assumed that the probability of interactions between two surfaces is proportional to the prevalence of said surfaces in the bulk system. Because [110]-[100] interactions have not been computed explicitly, the frequently invoked geometric mean approximation from values for [110]-[110] and [100]-[100] interactions is used. While more information regarding the method is provided in SI (Section S13), the results are shown in Table 1. PMF values fluctuate within ± 1 kcal/mol in all aqueous phases considered, at surface separation distances >1 nm. Normalised over the interfacial areas of the surface pairs, this translates

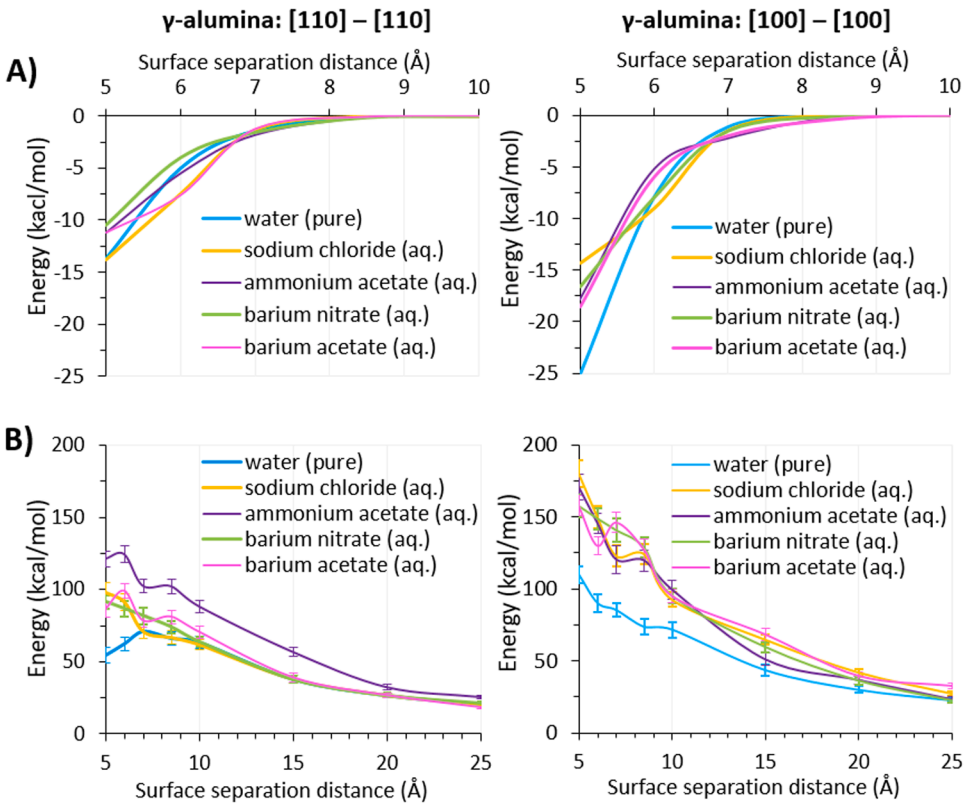

Fig. 7. Decomposition of γ-alumina [110] and [100] surface interactions into van der Waals and Coulomb potentials (rows A and B, respectively) as a function of surface separation distance, in pure water and aqueous salt solutions. First and second columns show [110]-[110] and [100]-[100] surface interactions, respectively. In the Coulomb plots, error bars represent standard deviation of the data point values. Corresponding error bars for the van der Waals plots are too small for graphical representation. The lines are guides to the eye. All salt solutions are at 1 molar concentration, except for barium nitrate (at 0.3 molar).

Table 1
Effective work of cohesion per unit area between γ-alumina nanoparticles in pure water and aqueous salt solutions, obtained from simulation results. All salt solutions are at 1 molar concentration, except for barium nitrate (0.3 molar). Uncertainties are of at least 0.26 mJ/m^2.

Aqueous phase	Work of cohesion per unit area (mJ/m^2)
sodium chloride	0.16
barium nitrate	0.55
ammonium acetate	0.77
water	1.22
barium acetate	1.50

to uncertainties of ± 0.24 and 0.31 mJ/m^2 in $W_{cohesion}$ values for [110] and [100] surface interactions respectively; or ~0.26 mJ/m^2 if applied to the values in Table 1 with the corresponding weightings. It is however recognized that PMF profiles for interactions between [100] and [110] surfaces are not available, thereby contributing additional uncertainty to the results shown in Table 1.

In Table 1, the average values for interparticle work of cohesion in all the salt solutions are lower than the values in pure water, with the exception of barium acetate. From SI, Table S4, we also note that, in all the aqueous phases, work of cohesion values between [110] surfaces are weaker compared to [100]; with the marginal exception of barium acetate. The weaker [110] interactions could reflect - at least partly - the atomistic-scale roughness of this surface, discussed in previous work [30]. Surface roughness at these smallest scales has been shown to be a critically important influence on surface tension, and on contact and adhesion of soft materials to rough surfaces [91,92].

From Table 1, it can be seen that the average interparticle $W_{cohesion}$ values increase in the order: sodium chloride < barium nitrate < ammonium acetate < water < barium acetate. Because the values in Table 1 represent the reversible thermodynamic work required to *separate* two adherent surfaces to a large distance, the largest agglomerates would be expected to occur in presence of barium acetate. However, it is worth considering that the values of Table 1 integral-out the features of the free-energy landscapes, which are shown in Fig. 2. Because the formation of agglomerates involves particles *approaching* each other, under quiescent conditions, sizeable free-energy barriers would determine the distance of closest approach. For example, considering [100] interactions in aqueous solution of barium acetate (Fig. 2, Panel B); the work required to leave the free-energy minimum at 9 Å reduces the likelihood of any closer approach between those surfaces. This argument is exploited in SI, Fig. S14, to illustrate the extraction of distances of closest approach from the PMF profiles.

4.2. Experimental results: particle agglomeration

DLS experiments were conducted for aqueous dispersions containing y-alumina particles of size < 50 nm (see SI, Table S1 for complete experimental details). Because agglomeration between specific crystallographic faces cannot be parsed, it is assumed that, consistent with literature observations [35–37], the particles used in this study provide a ~ 70:30 % exposure mix of [110] and [100] surfaces, respectively [35–37]. The DLS results are presented in Table 2 as the arithmetic mean of three measurements for each sample. Compared to results obtained in pure water, all the ion pairs induce particle agglomeration, as shown by the increases in hydrodynamic diameter. The effect is stronger in the order: barium nitrate < barium acetate < ammonium acetate < sodium chloride, with a corresponding decrease in diffusion coefficients measured experimentally.

This ranking can be interpreted by collectively considering the PMF profiles (Fig. 2) of the [110]-[110] and [100]-[100] interactions. In aqueous solutions containing barium acetate, the PMF profiles show features more accentuated relative to those observed in pure water, but located at similar surface-surface separations. This suggests that the size, charge distribution complexity and divalence of barium acetate reinforces the hydration structures within the lubrication film. The PMF profiles obtained in the presence of ammonium acetate lie between this

Table 2
Mean hydrodynamic diameter of γ-alumina nanoparticle agglomerates in pure water and aqueous salt solutions, as determined by DLS. Polydispersity and diffusion coefficients of particles in suspension are also shown. The results show that in aqueous solution, all ion pairs considered induce nanoparticle agglomeration, relative to pure water.

Aqueous phase	Hydrodynamic diameter (nm)	Polydispersity	Diffusion coefficient (cm^2/s)
water (pure)	**800.94**	**0.191**	**5.410E-09**
Std Err:	40.79	0.018	2.910E-10
Std Dev:	91.20	0.041	6.506E-10
sodium chloride (1 molar)	**3917.85**	**0.160**	**1.096E-09**
	105.82	0.045	5.216E-11
Std Err:	183.29	0.078	3.016E-10
Std Dev:			
ammonium acetate (1 molar)	**2922.64**	**0.09**	**1.467E-09**
	36.959	0.004	1.545E-11
	64.015	0.008	6.188E-11
Std Err:			
Std Dev:			
barium nitrate (0.3 molar)	**1207.78**	**0.275**	**3.753E-09**
	140.62	0.119	3.253E-10
Std Err:	314.44	0.266	1.627E-09
Std Dev:			
barium acetate (1 molar)	**1507.97**	**0.078**	**2.844E-09**
	24.42	0.056	1.642E-11
Std Err:	42.30	0.096	7.850E-11
Std Dev:			

scenario, and the 'flatness' of the PMF profiles obtained in the presence of sodium chloride. Sodium and chloride ions are found to approach closest to the surfaces compared to the rest of the ion pairs considered here. The resulting PMF profiles show no significant free-energy barriers prohibiting the approach between the particle surfaces. Because of its lower water solubility, barium nitrate was present at 0.3 molar. If salt effects were dependent solely on concentration, we might expect barium nitrate to have the smallest effect on particle agglomeration of the salts considered; which it does (Table 2). However, the variation of results between the salt solutions at equal concentration (1 molar) show that concentration alone does not determine the magnitude of effect, as widely accepted in the field. As we discussed previously for bulk aqueous solutions [34], an ion-pair with higher valence, greater steric impacts and more populous hydration-shells (all interlinked attributes) will exert, at lower aqueous concentration, the same or possibly stronger influence on observables reflecting these attributes, compared to a salt at higher concentration with weaker characteristics for the aforementioned attributes. We anticipate such attributes to manifest in observables reflecting salt-specific effects on interaction free-energy topologies. Shown in Table 3, and discussed below, we further demonstrate that these observables show negative correlation with agglomerate size.

To better understand the relationship between free-energy topologies and our experimental results, we compute the work of cohesion following an alternative approach. The results are referred to as $W_{cohesion}$''. For each force-distance curve, we integrate over the minimum that intuitively appears as the most energetically probable surface separation distance (details in SI, Section S14). The weighting procedure of SI, Section S13 is applied to extract $W_{cohesion}$''. The likely interparticle separation distance is obtained from values extracted separately for [110]-[110] and [100]-[100] PMFs as described in SI, Section S15: Tables S5 and S6. The results are shown in Table 3.

Table 3
Effective $W_{cohesion}$'' per unit area (simulation derived) between γ-alumina nanoparticles in pure water and aqueous salt solutions, obtained from simulation results. Average interparticle separation distances in each aqueous solution (simulation derived) are also shown. All salt solutions are at 1 molar concentration, except for barium nitrate (0.3 molar).

	$W_{cohesion}$'' per unit area (mJ/m^2)	Average interparticle separation distance (Å)
sodium chloride	0.18	6.5
water (pure)	0.97	7.7
ammonium acetate	1.14	7.8
barium acetate	1.64	8.25
barium nitrate	0.27	7.2–10

While the $W_{cohesion}$'' values are different compared to the data shown in Table 1, the ranking is broadly the same; except for the position swap of results obtained in pure water and in the presence of ammonium acetate. The results in Table 3 show that barium nitrate, although present at a lower concentration, yields somewhat greater values for $W_{cohesion}$'' and average interparticle separation distance than sodium chloride. Both these observables, particularly the latter, give an indication of the steric impact for each ion-pair in the context of particle agglomeration under quiescent conditions.

In Fig. 8 we explore correlations between experimental results (Table 2) and data shown in Table 3 for systems containing ion pairs at 1 molar (results including also barium nitrate, at 0.3 molar, are shown in SI, Section S16). Both the energetically probable separation distance and 'work of cohesion' between particles increases with structural complexity of the ion-pair (Fig. 8, panel A). The experimental agglomerate size decreases as the ion pairs become more structurally complex, in terms of both average equilibrium separation distance (Fig. 8, panel B) and $W_{cohesion}$'' (Fig. 8, panel C). This suggests that in aqueous solution, salt-specific effects on agglomeration for the systems considered manifest through modifying the features of the free-energy profiles, relative to those obtained in pure water. Our results suggest that the free energy barriers encountered by the surfaces as they approach each other in solution are more important than the overall work of cohesion in determining the hydrodynamic radius of aggregates in quiescent conditions.

Finally, we note from Tables 1 and 3 that, on average, the results for interactions in pure water lie between barium acetate and the rest of the ion pairs. This is of interest, as the results above are interpreted based on the structure of hydration water on the alumina substrate. In prior work, the hydration structure on the ion pairs was shown to correlate with the dynamical properties of water, and, out of the ions considered in the present work, barium acetate was found to have the strongest effect on water dynamics [34]. Therefore, it is possible that, while hydration water on the solid substrates is the primary reasons for changes in the hydrodynamic radius, the hydration structure of the ion pairs themselves is also important. The competition between these two phenomena is possibly responsible for the discrepancy between experimental and simulated data for agglomerates in pure water. Namely, because experimentally the agglomerates were the smallest in pure water, one could have expected largest $W_{cohesion}$ data for this system, which is not the case.

5. Conclusions

The aim of this work was to quantify interactions between γ-alumina particles in pure water and dilute aqueous salt solutions. This was done using a two-pronged approach at very different resolutions; atomistic molecular dynamics simulations and dynamic light scattering (DLS) experiments.

Using MD simulations, we differentiated interaction characteristics of the two predominantly exposed crystallographic terminations of γ-alumina; [110] and [100]. At surface separation distances of <1.5 nm, i.e., the 'contact zone', interactions between [110] surfaces were found to yield flatter potential of mean force profiles, in both pure water and the aqueous salt solutions, compared to [100]-[100] interactions. This trend was linked to the intrinsic differences between the [110] and [100] terminations. Within the 'contact zone' of [110]-[110] interactions, water was found to be arranged in narrower hydration layers.

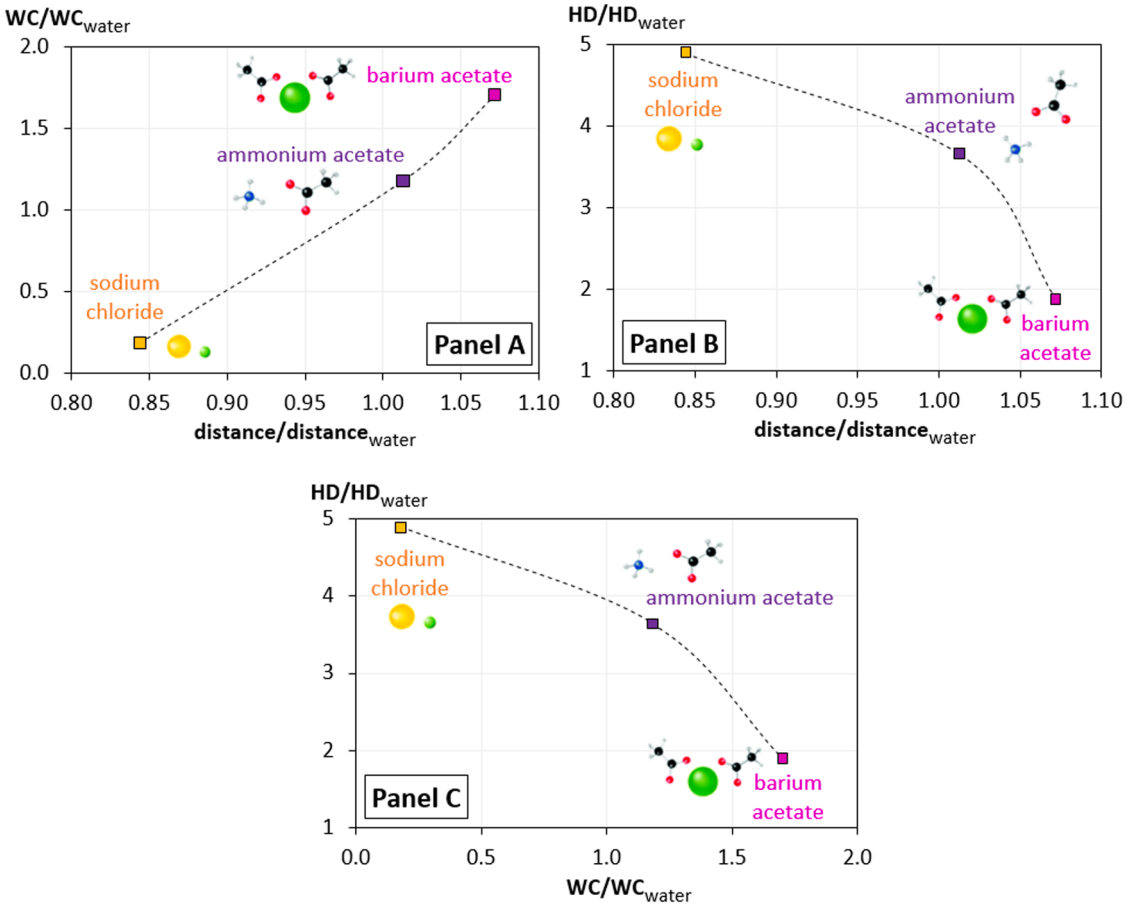

Fig. 8. Correlations between agglomerate size, cohesive work ($W_{cohesion}$'') per unit area, and energetically probable surface separation distance for γ-alumina nanoparticles in aqueous salt solutions, normalised relative to results in pure water. Panel A: $W_{cohesion}$'' per unit area (WC) vs. separation distance. Panel B: hydrodynamic diameter (HD) vs. separation distance. Panel C: hydrodynamic diameter vs. $W_{cohesion}$'' per unit area (WC). Experimental systems are considered under quiescent conditions.

By contrast, the lubrication film between [100] surfaces comprised fewer, thicker hydration layers. Interactions between [100] surfaces showed greater sensitivity to the presence of ions in solution. In fact, ion pairs were found closer to the [100] surfaces, as opposed to [110], for which ions were distributed mostly towards the centre of the lubricating aqueous film. All the ion pairs were found to enhance electrostatic repulsion between the surfaces, relative to pure water, at surface separations less than 2 nm. This effect was more pronounced for ion pairs that reside, on average, closer to the surfaces. The simulation results suggested that sodium chloride, out of the ion pairs considered, is most likely to induce particle agglomeration, as it reduces the free-energy barriers observed in the PMF profiles relative to interactions in pure water. This interpretation was supported by the results of our DLS experiments. All the salts were found to induce particle agglomeration, relative to pure water, with pronounced salt-specific effects. A correlation was found between experimental hydrodynamic radii and features of the PMF profiles related to the presence of strong repulsive peaks. Of note, the range of interaction considered in the present work is mostly within the domain of 'short-range' hydration forces. Considered together, our simulation results and macroscopic experimental findings suggest that these forces have an extensive impact on macroscopic observables.

CRediT authorship contribution statement

Striolo and Sarwar are responsible for the conceptualization of the research presented in this work. Drecun is responsible for simulation and experimental methodology. Bernardini is responsible for experimental methodology. Drecun is responsible for Visualization. Striolo, Sarwar, and Bernardini are responsible for securing resources. Drecun is responsible for Writing the original draft. All Authors are responsible for editing and revising the draft. Striolo is responsible for funding acquisition. Striolo, Sarwar and Bernardini are responsible for Project administration.

Declaration of Competing Interest

The authors declare no conflict of interest.

Data Availability

Data will be made available on request.

Acknowledgments

This project was supported financially, in part, by Johnson Matthey. Computational time and resources were provided by University College London Research Computing Platforms Support (Young and Kathleen clusters). We are grateful to the UK Materials and Molecular Modelling Hub for computational resources, which is partially funded by EPSRC (EP/P020194/1 and EP/T022213/1). Very special thanks go to Dr. Han Wu (research laboratories manager at the Centre for Nature-Inspired Engineering at UCL Dept. Chemical Engineering) for use of DLS facilities, and Xueming Xia (Research Instrument Technician, UCL Dept.

Chemical Engineering) for guidance on the DLS experiments. Many thanks go to Dr Anh Phan (formerly at UCL, Dept. Chemical Engineering; now at Dept. Chemical & Process Engineering, University of Surrey) for guidance and discussion on derivation of cohesive work from PMF profiles. AS is grateful for financial support to the Asahi Glass Chair in Chemical Engineering at the University of Oklahoma.

Supporting information

Simulation setup, protocols and analysis tools, and additional analyses (. PDF), together with determination of sample preparation accuracy for DLS experiments (. XLSX).

Appendix A. Supporting information

Supplementary data associated with this article can be found in the online version at doi:10.1016/j.colsurfa.2023.132152.

References

[1] D.T. Dan, Nanotechnology, nanoparticles and nanoscience: a new approach in chemistry and life sciences, Soft Nanosci. Lett. 10 (2020) 17–26.
[2] R. Gupta, H. Xie, Nanoparticles in daily life: applications, toxicity and regulations, J. Environ. Pathol. Toxicol. Oncol. 37 (2018) 209–230.
[3] W.J. Stark, P.R. Stoessel, W. Wohlleben, A. Hafner, Industrial applications of nanoparticles, Chem. Soc. Rev. 44 (2015) 5793–5805.
[4] S. Lu, R.J. Pugh, E. Forssberg, Chapter 5: industrial suspensions, Studies in Interface Science (Part. Vol.: Interfacial Sep. Part.) 20 (2005) 245–289.
[5] M.G. Rasteiro, A. Jorge, The influence of particle size distribution on the performance of ceramic particulate suspensions, Part. Part. Syst. Charact. 24 (2007) 101–107.
[6] L.L. Schramm, Suspensions: basic principles, Adv. Chem. 251 (1996) 3–44.
[7] A. Singer, Z. Barakat, S. Mohapatra, S.S. Mohapatra, Chapter 13 - Nanoscale drug-delivery systems: in vitro and in vivo characterization, Nanocarriers Drug Deliv.: Nanosci. Nanotechnol. Drug Deliv. (a Vol. Micro Nano Technol.) (2019) 395–419.
[8] D. Jung, M.J. Uttinger, P. Malgaretti, W. Peukert, J. Walter, et al., Hydrodynamic simulations of sedimenting dilute particle suspensions under repulsive DLVO interactions, Soft Matter 18 (2022) 2157–2167.
[9] J. Vesaratchanon, A. Nikolov, D.T. Wasan, Collective particle interactions in the sedimentation of charged colloidal suspensions, Ind. Eng. Chem. Res. 48 (2009) 80–84.
[10] E.J. Hinch, An averaged-equation approach to particle interactions in a fluid suspension, J. Fluid Mech. 83 (1977) 695–720.
[11] A. Otsuki, G. Bryant, Characterization of the interactions within fine particle mixtures in highly concentrated suspensions for advanced particle processing, Adv. Colloid Interface Sci. 226 (Part A) (2015) 37–43.
[12] K. Yeo, M.R. Maxey, Simulation of concentrated suspensions using the force-coupling method, J. Comp. Phys. 229 (2010) 2401–2421.
[13] T. Traverso, S. Michelin, Hydrochemical interactions in dilute phoretic suspensions: From individual particle properties to collective organization, Phys. Rev. Fluids 5 (2020), 104203.
[14] D. Vollath, Criteria ruling particle agglomeration, Beilstein J. Nanotechnol. 12 (2021) 1093–1100.
[15] T. Tadros, Interparticle interactions in concentrated suspensions and their bulk (Rheological) properties, Adv. Colloid Interface Sci. 168 (2011) 263–277.
[16] R. Massaro, G. Colombo, P.V. Puyvelde, J. Vermant, Viscoelastic cluster densification in sheared colloidal gels, Soft Matter 16 (2020) 2437–2447.
[17] B. Xia, P.S. Krueger, Rheology of particulate suspensions with non-Newtonian fluids in capillaries, Proc. R. Soc. A 478 (2022), 20210615.
[18] M. Urbonavicius, S. Varnagiris, L. Pranevicius, D. Milcius, Production of gamma alumina using plasma-treated aluminum and water reaction byproducts, Materials 13 (2020) 1300.
[19] K. Ishaq, A.A. Saka, A.O. Kamardeen, A. Abdulrahman, I.K. Adekunle, A. S. Afoldabi, Application of γ-alumina as catalyst support for the synthesis of CNTs in a CVD reactor, Adv. Nat. Sci.: Nanosci. Nanotechnol. 9 (035012) (2018) 16p.
[20] M. Trueba, S.P. Trasatti, γ-Alumina as a support for catalysts: a review of fundamental aspects, Eur. J. Inorg. Chem. 17 (2005) 3393–3403.
[21] G. Busca, The surface of transitional aluminas: a critical review, Catal. Today 226 (2014) 2–13.
[22] J. Mui, J. Ngo, B. Kim, Aggregation and colloidal stability of commercially available al2o3 nanoparticles in aqueous environments, Nanomaterials 6 (2016) 90.
[23] R. Mondragón, J. Enrique Juliá, L. Cabedo, N. Navarrete, On the relationship between the specific heat enhancement of salt-based nanofluids and the ionic exchange capacity of nanoparticles, Sci. Rep. 8 (2018) 7532.
[24] H. Rehman, M. Batmunkh, H. Jeong, H. Chung, Sedimentation study and dispersion behavior of Al2O3–H2O nanofluids with dependence of time, Adv. Sci. Lett. 6 (2012) 96–100.
[25] S. Witharana, C. Hodges, D. Xu, X. Lai, Y. Ding, Aggregation and settling in aqueous polydisperse alumina nanoparticle suspensions, J. Nanopart. Res. 14 (2012) 851.
[26] S.U. Ilyas, R. Pendyala, N. Marneni, Stability and agglomeration of alumina nanoparticles in ethanol-water mixtures, Procedia Eng. 148 (2016) 290–297.
[27] S. Manjula, S.M. Kumar, A.M. Raichur, G.M. Madhu, R. Suresh, M.A.L.A. Raj, A sedimentation study to optimize the dispersion of alumina nanoparticles in water, Cerâmica 51 (2005) 121–127.
[28] E. Firlar, S. Çınar, S. Kashyap, et al., Direct visualization of the hydration layer on alumina nanoparticles with the fluid cell STEM in situ, Sci. Rep. 5 (2015) 9830.
[29] C. Gerardi, D. Cory, J. Buongiorno, L.-W. Hu, T. McKrell, Nuclear magnetic resonance-based study of ordered layering on the surface of alumina nanoparticles in water, Appl. Phys. Lett. 95 (2009), 253104.
[30] O. Drecun, A. Striolo, M. Sarwar, C. Bernardini, Hydration structures on γ-alumina surfaces with and without electrolytes probed by atomistic molecular dynamics simulations, J. Phys. Chem. B 126 (2022) 9105–9122.
[31] G. Åkerlöf, A study of the composition of the liquid phase in aqueous systems containing strong electrolytes of higher valence types as solid phases, J. Phys. Chem. 41 (1937) 1053–1076.
[32] M. Aghaie, H. Aghaie, A. Ebrahimi, Thermodynamics of the solubility of barium nitrate in the mixed solvent, ethanol + water, and the related ion-association, J. Mol. Liq. 135 (2007) 72–74.
[33] R. Wright, Selective solvent action. Part VI. The effect of temperature on the solubilities of semi-solutes in aqueous alcohol, J. Chem. Soc. (1927) 1334–1337.
[34] O. Drecun, A. Striolo, C. Bernardini, Structural and dynamic properties of some aqueous salt solutions, Phys. Chem. Chem. Phys. 23 (2021) 15224–15235.
[35] M. Digne, P. Sautet, P. Raybaud, P. Euzen, H. Toulhoat, Use of DFT to achieve a rational understanding of acid-basic properties of gamma-alumina surfaces, J. Catal. 226 (2004) 54–68.
[36] J.-P. Beaufils, Y. Barbaux, Détermination, par diffraction différentielle de neutrons, des faces cristallines exposées par des supports de catalyseurs en poudre, J. Chim. Phys. 78 (1981) 347–352.
[37] P. Nortier, P. Fourre, A.B. Mohammed Saad, O. Saur, J.C. Lavalley, Effects of crystallinity and morphology on the surface properties of alumina, in: Applied Catalysis, 61, 1990, pp. 141–160.
[38] A. Zen, T. Bui, T.T.B. Le, W.J. Tay, K. Chellappah, et al., Long-range ionic and short-range hydration effects govern strongly anisotropic clay nanoparticle interactions, J. Phys. Chem. C 126 (2022) 8143–8151.
[39] G. Mancardi, M. Alberghini, N. Aguilera-Porta, M. Calatayud, P. Asinari, E. Chiavazzo, Multi-scale modelling of aggregation of TiO2 nanoparticle suspensions in water, Nanomaterials 12 (2022) 217.
[40] S. Jenkins, S.R. Kirk, M. Persson, J. Carlen, Z. Abbas, Molecular dynamics simulation of nanocolloidal amorphous silica particles: Part II, J. Chem. Phys. 128 (2008), 164711.
[41] H.O. Ayoola, S.D. House, C.S. Bonifacio, K. Kisslinger, W.A. Saidi, J.C. Yang, Evaluating the accuracy of common γ-Al2O3 structure models by selected area electron diffraction from high-quality crystalline γ-Al2O3, Acta Mater. 182 (2020) 257–266.
[42] N.M. Stuart, K. Sohlberg, The microstructure of γ-alumina, Energies (2021), 14.
[43] P. Raybaud, C. Chizallet, C. Mager-Maury, M. Digne, H. Toulhoat, P. Sautet, From γ-alumina to supported platinum nanoclusters in reforming conditions: 10 years of DFT modeling and beyond, J. Catal. 308 (2013) 328–340.
[44] L. Cheng, T. Xu, W. Li, Z. Chen, J. Ai, Z. Zhou, J. Liu, Density functional theory investigation into the B and Ga doped clean and water covered γ-alumina surfaces, J. Chem. (2017). Article ID 6215315, 7 pages.
[45] R. Wischert, P. Laurent, C. Copéret, F. Delbecq, P. Sautet, γ-alumina: the essential and unexpected role of water for the structure, stability, and reactivity of "Defect" sites, J. Am. Chem. Soc. 134 (2012) 14430–14449.
[46] X. Tan, X. Ren, X. Wang, Theoretical investigation of uranyl ion adsorption on hydroxylated γ-Al2O3 surfaces, RSC Adv. 3 (2013) 19551–19559.
[47] H. Wang, L. Chen, Y. Lv, R. Ren, H2 dissociation on γ-Al2O3 supported Cu/Pd atoms: a DFT investigation, Appl. Surf. Sci. 290 (2014) 154–160.
[48] R.-P. Ren, X.-W. Liu, Y.-K. Lv, Theoretical investigation of H2S removal on γ-Al2O3 surfaces of different hydroxyl coverage, RSC Adv. 5 (2015) 55372–55382.
[49] J. Gu, J. Wang, J. Leszczynski, Single site Fe on the (110) surface of γ-Al2O3: insights from a DFT study including the periodic boundary approach, Phys. Chem. Chem. Phys. 23 (2021) 7164–7177.
[50] J. Gu, J. Wang, J. Leszczynksi, Structure and energetics of (111) surface of γ-Al2O3: insights from DFT including periodic boundary approach, ACS Omega 3 (2018) 1881–1888.
[51] B.F. Ngouana-Wakou, P. Cornette, M. Corral Valero, D. Costa, P. Raybaud, An atomistic description of the γ-alumina/water interface revealed by Ab initio molecular dynamics, J. Phys. Chem. C 121 (2017) 10351–10363.
[52] R. Réocreux, É. Girel, P. Clabaut, A. Tuel, M. Besson, A. Chaumonnot, A. Cabiac, P. Sautet, C. Michel, Reactivity of shape-controlled crystals and metadynamics simulations locate the weak spots of alumina in water, Nat. Commun. (2019), 10.
[53] R. Réocreux, T. Jiang, M. Iannuzzi, C. Michel, P. Sautet, Structuration and dynamics of interfacial liquid water at hydrated γ-alumina determined by ab initio molecular simulations: implications for nanoparticle stability, ACS Appl. Nano Mater. 1 (2018) 191–199.
[54] A.R. Ferreira, E. Küçükbenli, S. de Gironcoli, W.F. Souza, S.S.X. Chiaro, E. Konstantinova, A.A. Leitão, Structural models of activated γ-alumina surfaces revisited: Thermodynamics, NMR and IR spectroscopies from ab initio calculations, Chem. Phys. 423 (2013) 62–72.

[55] R.T. Cygan, J.J. Liang, A.G. Kalinichev, Molecular models of hydroxide, oxyhydroxide, and clay phases and the development of a general force field, J. Phys. Chem. B. 108 (2004) 1255–1266.
[56] F. Chen, Q. Ding, X. Wang, H. Wang, L. Zhang, High-loading washcoat of γ-alumina on FeCrAlloy mesh with acid-free slurry, Surf. Coat. Technol. 403 (2020), 126394.
[57] N.R. Peela, A. Mubayi, D. Kunzru, Washcoating of γ-alumina on stainless steel microchannels, Catal. Today 147 (2009) S17–S23.
[58] H.J.C. Berendsen, J.R. Grigera, T.P. Straatsma, The missing term in effective pair potentials, J. Phys. Chem. 91 (1987) 6269–6271.
[59] J.P. Ryckaert, G. Ciccotti, H.J.C. Berendsen, Numerical integration of the Cartesian equations of motion of a system with constraints: molecular dynamics of n-Alkanes, J. Com. Phys. 23 (1977) 327–341.
[60] S. Plimpton, Fast parallel algorithms for short-range molecular dynamics, J. Comp. Phys. 117 (1995) 1–19. ⟨http://lammps.sandia.gov⟩.
[61] Particle-Particle-Particle-Mesh (P3M) Algorithms, 267-304. Computer simulation using particles, Hockney, R.W., Eastwood, J.W, CRC Press, 1988. ISBN: 9780852743928.
[62] H.A. Lorentz, Ueber die Anwendung des Satzes vom Virial in der kinetischen Theorie der Gase, Ann. der Phys. 248 (1881) 127–136.
[63] D. Berthelot, Sur le mélange des gaz, Comptes rendus Hebd. Des. séances De. l'Académie Des. Sci. 126 (1898) 1703–1855.
[64] W.C. Swope, H.C. Andersen, P.H. Berens, K.R. Wilson, A computer simulation method for the calculation of equilibrium constants for the formation of physical clusters of molecules: application to small water clusters, J. Chem. Phys. 76 (1982) 637–649.
[65] S. Nosé, A molecular dynamics method for simulations in the canonical ensemble, Mol. Phys. 52 (1984) 255–268.
[66] W.G. Hoover, Canonical dynamics: equilibrium phase-space distributions, Phys. Rev. A. 31 (1985) 1695–1697.
[67] G.M. Torrie, J.P. Valleau, Nonphysical sampling distributions in Monte Carlo free-energy estimation: umbrella sampling, J. Comp. Phys. 23 (1977) 187–199.
[68] G.M. Torrie, J.P. Valleau, Monte Carlo free energy estimates using non-Boltzmann sampling: Application to the sub-critical Lennard-Jones fluid, Chem. Phys. Lett. 28 (1974) 578–581.
[69] G. Fiorin, M.L. Klein, J. Henin, Using collective variables to drive molecular dynamics simulations, Mol. Phys. 111 (2013) 3345–3362.
[70] S. Kumar, J.M. Rosenberg, D. Bouzida, R.H. Swendsen, P.A. Kollman, The weighted histogram analysis method for free-energy calculations on biomolecules. I. The method, J. Comp. Chem. 13 (1992) 1011–1021.
[71] Grossfield. A. Wham: The Weighted Histogram Analysis Method (Software), available at: http://membrane.urmc.rochester.edu/?page_id=126 [Accessed: 7th May 2022).
[72] J. Stetefeld, S.A. McKenna, T.R. Patel, Dynamic light scattering: a practical guide and applications in biomedical sciences, Biophys. Rev. 8 (2016) 409–427.
[73] Einstein, A. Über die von der molekularkinetischen Theorie der Wärme geforderte Bewegung von in ruhenden Flüssigkeiten suspendierten Teilchen. Annalen der Physik (in German), 1905, 322, 549–560. https://doi.org/10.1002/andp.19053220806 English translation (Dover publications, Inc.,) available at: https://www.maths.usyd.edu.au/u/UG/SM/MATH3075/r/Einstein_1905.pdf [Accessed: 25th August, 2022].
[74] Z.S. Artemyeva, N.P. Kirillova, N.N. Danchenko, B.M. Kogut, E.B. Taller, The study of physical and chemical characteristics of organo-clay complexes of the chronosequence of albic retisols using dynamic light scattering and phase analysis light scattering, Eurasia Soil Sci. 53 (2020) 446–453.
[75] D. Argyris, A. Phan, A. Striolo, P.D. Ashby, Hydration structure at the α-Al2O3 (0001) surface: insights from experimental atomic force spectroscopic data and atomistic molecular dynamics simulations, J. Phys. Chem. C 117 (2013) 10433–10444.
[76] A. Klaasen, F. Liu, F. Mugele, I. Siretanu, Correlation between electrostatic and hydration forces on silica and gibbsite surfaces: an atomic force microscopy study, Langmuir 38 (2022) 914–926.
[77] A. Striolo, A.A. Chialvo, P.T. Cummings, K.E. Gubbins, Water adsorption in carbon-slit nanopores, Langmuir 19 (2003) 8583–8591.
[78] V. Mazzini, V.S.J. Craig, Correction: what is the fundamental ion-specific series for anions and cations? Ion specificity in standard partial molar volumes of electrolytes and electrostriction in water and non-aqueous solvents, Chem. Sci. 10 (2019) 3430–3433, https://doi.org/10.1039/C9SC90050K Original article: Chem. Sci., 2017, 8, 7052-7065.
[79] CrystalMaker webpage: 'Elements, Atomic Radii and the Periodic Table', and references therein. URL: http://crystalmaker.com/support/tutorials/atomic-radii/index.html [Accessed: 23rd August 2022].
[80] CrystalMaker Element Tables: 'CPK Atomic-Ionic Radii', and references therein. URL: http://crystalmaker.com/support/tutorials/atomic-radii/resources/CPK_Atomic_Ionic_Radii.jpg [Accessed: 23rd August 2022].
[81] J.C. Slater, Atomic radii in crystals, J. Chem. Phys. 41 (1964) 3199–3204.
[82] B.V. Derjaguin, L. Landau, Theory of the stability of strongly charged lyophobic sols and of the adhesion of strongly charged particles in solutions of electrolytes (Available at), Acta Physicochim. URSS 14 (1941) 633, https://doi.org/10.1016/0079-6816(93)90013-L.
[83] E.J.W. Verwey, J.T.G. Overbeek, Book available at: http://www.damtp.cam.ac.uk/user/gold/pdfs/teaching/VerweyOverbeek.pdf [Accessed: 31st October, Theory of the Stability of Lyophobic Colloids, 1948, Elsevier, Amsterdam, 2022.
[84] B.R. Shrestha, X. Banquy, Hydration forces at solid and fluid biointerfaces, Biointerphases 11 (2016), 018907.
[85] V.A. Parsegian, T. Zemb, Hydration forces: observations, explanations, expectations, questions, Curr. Opin. Colloid Interface Sci. 16 (2011) 618–624.
[86] J.J. Valle-Delgado, J.A. Molina-Bolívar, F. Galisteo-González, F. Feiler, M. W. Rutland, Hydration forces between silica surfaces: experimental data and predictions from different theories, J. Chem. Phys. 123 (2005), 034708.
[87] LAMMPS: compute group/group command - LAMMPS documentation. URL: https://docs.lammps.org/compute_group_group.html [Accessed: 28th November 2022].
[88] R.M. Adar, T. Markovich, A. Levy, H. Orland, D. Andelman, Dielectric constant of ionic solutions: combined effects of correlations and excluded volume, J. Chem. Phys. 149 (2018), 054504.
[89] H. Gao, Y. Chang, C. Xiao, An analytical expression for the dielectric decrement law, AIP Adv. 10 (2020), 045109.
[90] D. Ben-Yaakov, D. Andelman, R. Podgornik, Dielectric decrement as a source of ion-specific effects, J. Chem. Phys. 134 (2011), 074705.
[91] S. Dalvi, A. Gujrati, S.R. Khanal, T.D.B. Jacobs, Linking energy loss in soft adhesion to surface roughness, PNAS 116 (2019) 25484–25490.
[92] B.N.J. Persson, O. Albohr, U. Tartaglino, A.I. Volokitin, E. Tosatti, On the nature of surface roughness with application to contact mechanics, sealing, rubber friction and adhesion, J. Phys.: Condens. Matter 17 (2005) R1–R62.